PNNL-32020

Modeling Induction Stirring and Particle Tracking in Molten Uranium

September 2021

David Abrecht
Jacob Bair
Jordan Corbey
Nikhil Deshmukh
William Frazier
Amanda Howard
Shenyang Hu
Rajesh Singh

Prepared for the U.S. Department of Energy
under Contract DE-AC05-76RL01830

PACIFIC NORTHWEST NATIONAL LABORATORY
operated by
BATTELLE
for the
UNITED STATES DEPARTMENT OF ENERGY
under Contract DE-AC05-76RL01830

Printed in the United States of America

Available to DOE and DOE contractors from the
Office of Scientific and Technical Information,
P.O. Box 62, Oak Ridge, TN 37831-0062;
ph: (865) 576-8401
fax: (865) 576-5728
email: reports@adonis.osti.gov

Available to the public from the National Technical Information Service
5301 Shawnee Rd., Alexandria, VA 22312
ph: (800) 553-NTIS (6847)
email: orders@ntis.gov <https://www.ntis.gov/about>
Online ordering: http://www.ntis.gov

PNNL-32020

Modeling Induction Stirring and Particle Tracking in Molten Uranium

September 2021

David Abrecht
Jacob Bair
Jordan Corbey
Nikhil Deshmukh
William Frazier
Amanda Howard
Shenyang Hu
Rajesh Singh

Prepared for
the U.S. Department of Energy
under Contract DE-AC05-76RL01830

Pacific Northwest National Laboratory
Richland, Washington 99354

Abstract

Two independent numerical models have been developed to simulate the behavior of carbon impurities in molten uranium metal. Informed by experimental parameters, one model was created using the commercial software Star-CCM+ and compared with another developed using open-source codes, including OpenFOAM, Finite Element Method Magnetics (FEMM) and a First Passage Kinetic Monte Carlo (FPKMC) approach. The target experimental system features a 404 g uranium metal charge containing an average carbon concentration of 139 ppm,[1-2] which was melted in a vacuum induction furnace at 1400° C then resolidified. The microstructures of the uranium and its impurities before and after melting have been characterized and reported separately.[3-4] Prior to simulating the uranium-carbon system described, the numerical models were validated using a previously published nonradioactive experimental system, to ensure agreement with expected output values.[5] Focus has been placed on modeling velocity fields under induction stirring and impurity particle trajectories.

Summary

Computational models have been developed to simulate the behavior of carbon impurities in the molten phase of uranium metal during the casting process. An experimental system housed in the Radiochemical Processing Laboratory (RPL) at the Pacific Northwest National Laboratory (PNNL), which uses a vacuum induction furnace to melt and cast uranium metal and alloys up to 2 kg, was employed for this project to inform the computational efforts. 404 g of depleted uranium metal[1-2] were melted in a cylindrical zirconia crucible (1.60 inch inner diameter, 1.88 inch outer diameter, 3.60 inch depth, 0.25 inch bottom wall thickness) at a maximum temperature of 1400 °C, which was held for 15 min. The molten metal was cooled and solidified in its original crucible before sectioning for post-melt analysis. Experimental characterization details of the uranium and its impurities both before and after melting have been published elsewhere.[3-4]

To simulate the induction furnace system, a computational model has been built using the commercial software STAR-CCM+. This model tracks the movement of microparticles through the velocity field of the inductively mixed molten metal. Concurrently, a second model for the same system has been built using open-source computational tools for comparison. The latter capability uses OpenFOAM as the primary software to compute the flow and particle trajectories with momentum and heat source terms coming from the open-source Finite Element Method Magnetics (FEMM) software, which captures the physics of electromagnetic induction. Outputs from both the Star-CCM+ and OpenFOAM models were used to inform a First Passage Kinetic Monte Carlo (FPKMC) algorithm as an alternative means of tracking particle movement in the generated velocity fields. Multiple modeling approaches were investigated to improve confidence in the results while maintaining the transparency and flexibility that open-source software can provide.

Prior to modeling our targeted uranium casting system with uranium carbide impurities, both the Star-CCM+ and open-source models were validated using a previously published system tracking lighter-than-melt particles in Wood’s metal,[5] which is a low melting point alloy that can be melted by induction in air.

Acknowledgments

This research was supported by the Laboratory Directed Research and Development (LDRD) Program at the Pacific Northwest National Laboratory (PNNL).

Acronyms and Abbreviations

CFD	Computational Fluid Dynamics
EM	Electromagnetic
FEMM	Finite Element Method Magnetics
FPKMC	First Passage Kinetic Monte Carlo
ICF	Induction Crucible Furnace
LPT	Lagrangian Particle Tracking
PNNL	Pacific Northwest National Laboratory
RPL	Radiochemical Processing Laboratory
U	Uranium
UC	Uranium Carbide

Contents

Figures

Tables

1. Introduction

In processed metals, impurities can influence mechanical properties and performance, which can be beneficial, when controlled.[3,6,7] However, in uranium metal processing, uncontrolled reactions between system components in the extreme casting environment make carbon impurities extremely common.[1,2,8-23] While the resulting ceramic inclusions can increase hardness and tensile strength at low concentrations, their uncontrolled formation can lead to material heterogeneity, which can affect the quality and reproducibility of the uranium metal product.[9, 24-28] In uranium, carbon-containing inclusions have been linked to void formation and material fracture.[8-9,26, 27,29]

According to accepted phase diagrams, uranium monocarbide is the expected form of carbon in solid uranium metal when carbon is present at concentrations less than 5 wt.%.[15, 30-31] Nitrogen and oxygen atoms have also been reported to incorporate into the uranium monocarbide lattice.[15, 22, 30-32] While some metal carbides have been considered fairly insoluble in molten uranium, experiencing buoyancy due to their decreased density,[23-24] UC particles are thought to dissolve, at least in part, at molten uranium temperatures. However, a complete kinetic understanding of uranium carbides in uranium is still lacking[33-34] and is likely influenced by several factors including uranium charge size, cooling rate, and impurity concentrations.

Understanding ceramic impurities and how they form and migrate could lead to improved uranium material properties. Due, in part, to the high temperature and inert atmosphere involved in these operations, direct experimental observation of the behavior of inclusions during uranium casting operations is difficult to obtain in a meaningful way. Computational modeling and system simulations can provide insight into inclusion behaviors that can be linked to properties of the final, cooled material.

As a first step, this study targeted simulation of the molten phase of uranium during induction melting, with the possibility of second phase particle incorporation. While several models have been developed for examining the migration of particles in molten systems, they typically relied on thin film approximations to minimize eddy currents in the material and a uniform particle size distribution.[35-37] Previous research from our group has utilized phase-field modeling[38] and other computational methods[39-41] to better predict how carbides form and distribute in U matrices during casting and processing.[27] To the best of our knowledge, the models reported here are the first to track particles in the flow of an inductively mixed molten uranium system.

Simulations of flows in induction furnaces have been studied using various numerical methods over the past decade. The earliest studies disregarded particle inclusions and considered only the flow patterns.[42,43] The first simulations of particles in turbulent flow in an induction furnace were performed by Kirpo *et. al.*[44] using the Fluent software. These early models only induced drag, electromagnetic (EM) and buoyancy forces. This approach[44] was again used in OpenFOAM by Ščepanskis *et. al.,*[45] with lift, acceleration, and virtual mass forces added to the simulation. The importance of each of these forces was further considered by these same authors.[46] Later, Ščepanskis *et. al.*[5] compared the outputs of this mathematical modelling approach to experimental results from a small induction crucible furnace (ICF). That report comparing simulation and experiment using Wood's alloy provides a benchmark case for the current work, denoted by ICF2. Wood's alloy and Wood's metal are interchangeable terms in this report.

More recent work has focused specifically on particle motion in an ICF.[47-48] In steady state, the turbulent flow within the ICF is shown to have axial asymmetries in the averaged flow field due to the long-time-scale oscillations. It is important to take these long-term oscillations into account, as they dominate the particle movement.[47] Related recent work has also focused on the behavior of the free surface of the melt and the complicated interactions between the EM field, the flow pattern, and the surface shape.[49] Early work used a reciprocal process for calculating the interactions between the EM field and the free surface shape.[50] The free surface oscillation period can be found analytically to depend only on the crucible geometry when the Lorentz force is radial and constant.[51] More advanced results require an iterative approach coupling the EM forces and the hydrodynamic flow.[49, 52] The models reported here employ and integrate previously published computational approaches for application to a specific uranium system.

2. Technical Approach

The general steps required to simulate the effect of the induction furnace on the crucible and its contents are:

1. Simulation of the EM field to predict the eddy currents induced in the melt, which in turn produce the Joule heating and Lorentz force in the melt. Note that the Joule heating was not included in the scope of present work.

2. Computational fluid dynamics (CFD) using the melt's physical properties, such as density and viscosity, along with the computed Lorentz force from Step 1 is used to predict the melt flow field inside the crucible. This flow field is then further used to predict the particle/inclusion motion.

3. Particle motion tracking simulates the motion of particles (inclusions) in the flow field generated in Step 2.

Since experimental data for the electromagnetics and flow field are not available for our current setup with molten uranium, we rely up comparison of our two models (open source FEMM/OpenFOAM and commercial CFD software STAR-CCM+) and their outputs with a known ICF model from the literature by Ščepanskis *et. al.*[5] A basic parameter check of FEMM[53] against analytical solutions for a simple cylindrical geometry was also done (see Appendix A). FEMM is used to model eddy currents, and Python is used to link the FEMM and OpenFOAM models. Particle tracking was also done outside of OpenFOAM using the FPKMC algorithm in a code written for this project.

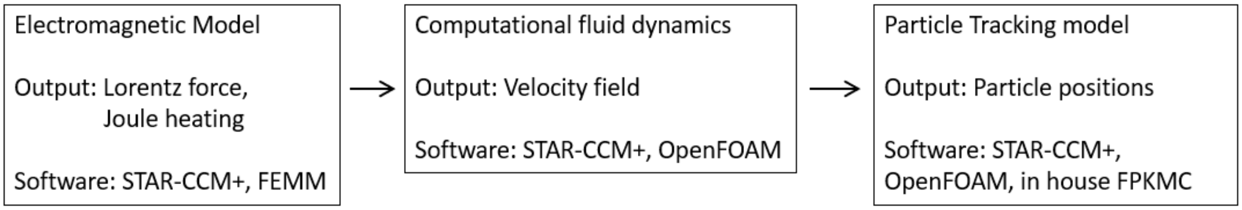

Figure 1. Schematic of model integration from open-source platforms and associated software.

Two major models/cases were dealt with in this work. One duplicates the ICF model from Ščepanskis *et. al.*[5] with Wood's alloy (called Ščepanskis ICF2, used for validating the modeling process) and the other models our laboratory setup with uranium (called Lab/Uranium setup.) The Lab/Uranium setup consists of an Indutherm vacuum tilting casting machine (VTC 200V Ti), as previously described.[1-2]

Outline of the custom modeling process:

1. FEMM is used to generate current density (J) and magnetic field (B) in the cylindrical melt in response to applied EM field from an induction coil.[1-2] FEMM cannot model a helical coil and approximates it with multiple circular coils. This approximation is expected to be quite good, except perhaps at the edges of the coil.

   FEMM interfaces with Python, which is used to extract the J and B fields from the FEMM model. The Python script is also used to generate the Lorentz force from the cross product of J and B. J and B are complex quantities that vary spatially in the melt and vary sinusoidally at 15 kHz (nominal operating frequency) over time. The spatially varying Lorentz force is written out on a regular cartesian grid in ASCII text format.

2. The custom OpenFOAM code and python are used to read in the Lorentz force from text files and interpolate it onto the mesh used for the CFD calculations. Both STAR-CCM+ and OpenFOAM CFD computations use the same mesh. The mesh is generated in STAR-CCM+ since it has easy-to-use mesh generation tools.

3. A modified version of the OpenFOAM pimpleFoam solver is used to compute the fluid velocities in the melt in response to the Lorentz force. The flow initially develops the expected rotational features within the fluid at the top and bottom of the crucible changes with time, possibly due to interaction between the top and bottom vortices. Good agreement between the FEMM/OpenFOAM, STAR-CCM+ models and the literature is obtained.

4. The OpenFOAM solver is also modified to include Lagrangian particle tracking to track inclusions. Particle tracking is also done in STAR-CCM+ and with an in-house code based on the FPKMC algorithm.

2.1 Analysis of UC Distribution in U Melt Pools by FPKMC Modeling

2.1.1 Model Description

In order to predict the effect of UC-UC interactions and the induction melting process on the spatial distribution of these carbides, a novel First Passage Kinetic Monte Carlo (FPKMC)[54] model of particle migration in molten U was developed. This method was designed to take as input the velocity field of the molten U, the modeling and simulation of which is described in earlier sections. The FPKMC method evolves a system of migrating defects by assuming that within a subsection of the simulation volume, sometimes referred to as a “protected” region, interaction between defects does not occur. Based on an analytical solution for the migration of the defect within that region with respect to time, the exit time and position of the defect can be stochastically generated. This advances the system clock. Using simple binary search methods, the exit time of the defect from its new protected region is sampled, and the motion of the modeled defects is simulated in chronological order. This method is advantageous in comparison to approaches in which all defects migrate in uniform time steps, because such a process requires $O(N^2)$ calculations to advance the clock, while the FPKMC method only requires $O(1)$ calculations for the migration of the defect and $O(N^{1/2})$ in order to correctly place migrating defects in order. This approach has largely been used to simulate the evolution of systems with reacting atomic species,[55-56] but in principle, this method can be applied to the simulation of the migration of larger defects.

2.1.2 UC Particle Migration

In the case of migrating UC particles within the U melt, buoyant force created by the difference between the density of the UC and the molten U must be considered along with the force exerted by the flowing molten U on the UC particles. To simplify this problem, we assume for this work that the U velocity field reaches a steady state under induction melting. We also assume that UC particles do not significantly affect the molten U velocity fields as they move, which allows our simulations to assume one-way coupling.[4, 57] This has the advantage that, at any given time, the necessary number of UC particles to simulate can be significantly smaller than the number likely present within the melt. For context into this problem, uranium ingots containing 10% molybdenum have been recently reported to have on the order of 1% of cross-sectional area contain UC, which corresponds to approximately 400 ppm C. However, UC particles in these cases were regularly 1 µm in diameter or less,[58-59] which suggests a particle density on the order of 10^{12} particles/m^3 or approximately 10^7 particles/in^3.

Accounting for the Brownian motion of the UC particles, we assume a protected region for each particle with width *l.* Given an equilibrium velocity, *v,* under the effects of drag and the buoyant force, the exit time from the protected region, *t*, can be determined by sampling from the standard normal distribution *N(0,1)*:

$$\boldsymbol{N(0,1)} = \frac{\boldsymbol{\Delta x - vt}}{\sqrt{\boldsymbol{Dt}}} \qquad \textbf{(1)}$$

Here, the diffusion coefficient due to Brownian motion, *D,* is calculated as a function of temperature, *T*, particle size *r*, and the viscosity of the molten metal, *µ*:

$$\boldsymbol{D} = \frac{\boldsymbol{k_B T}}{\boldsymbol{6\pi\mu r}} \qquad \textbf{(2)}$$

In these simulations, the protected region is cubic, so the exit time is the minimum sampled exit time for each dimension, *i where i=1,2,3,etc*:

$$\boldsymbol{t_{Exit}} = \boldsymbol{min_i}\ (\boldsymbol{t_{Exit,\,i}}) \qquad \textbf{(3)}$$

A schematic representation of this process is shown in Figure 2.

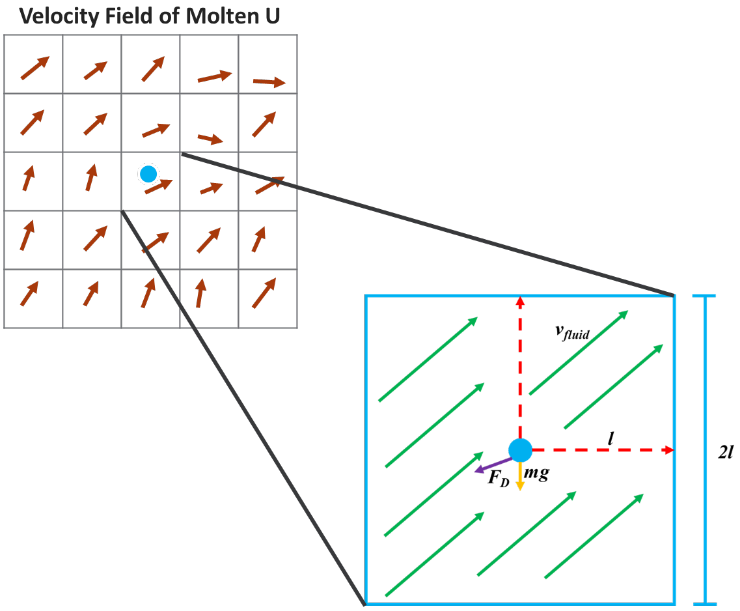

Figure 2. A schematic representation of a UC particle (blue circle) migrating within the molten U velocity field. The forces of drag and gravity exert force on the particle, which influences its exit from a region of length 2l used in FPKMC model.

2.1.3 Particle Collision Model

Simulations were performed to explore the effect of interparticle interaction on the distribution of UC particles within the U melt. Three possibilities were considered. In the first case, UC particles did not interact with each other. In the second case, UC particles were allowed to collide and exhibited perfectly elastic collisions. In the final case, UC particles were allowed to collide, but exhibited perfectly inelastic collisions. In this third case, it was assumed that agglomerating particles rapidly merge to form spherical particles. Collisions between individual particle pairs were determined on a stochastic basis. This was necessary because, as previously mentioned, one-way coupling did not require all particles to be directly simulated to ascertain the UC distribution as it evolved. Given a pair of moving particles with radii r_1 and r_2, with the first particle moving at a velocity v_1 relative to the second, the volume V_{Col} in which the second particle could be expected to collide with the first over some period, Δt, can be expressed as:

$$\boldsymbol{V_{Col} = \bar{v}_1 \Delta t \pi (r_1 + r_2)^2} \tag{4}$$

If the two particles exist within a volume, V, the probability of a single collision is simply V_{Col}/V. If each UC particle in the simulation is taken to represent n particles that exist in the experimental system, the probability that no collisions occur is:

$$\boldsymbol{p_0 = \left(1 - \frac{V_{Col}}{V}\right)^n} \tag{5}$$

The probability that at least one collision occurs is therefore the complement of this expression. In these cases, we assume that the time between UC jumps is small enough that multiple collisions do not occur between the same pair of carbides. A schematic representation of this calculation is shown in
Figure 3.

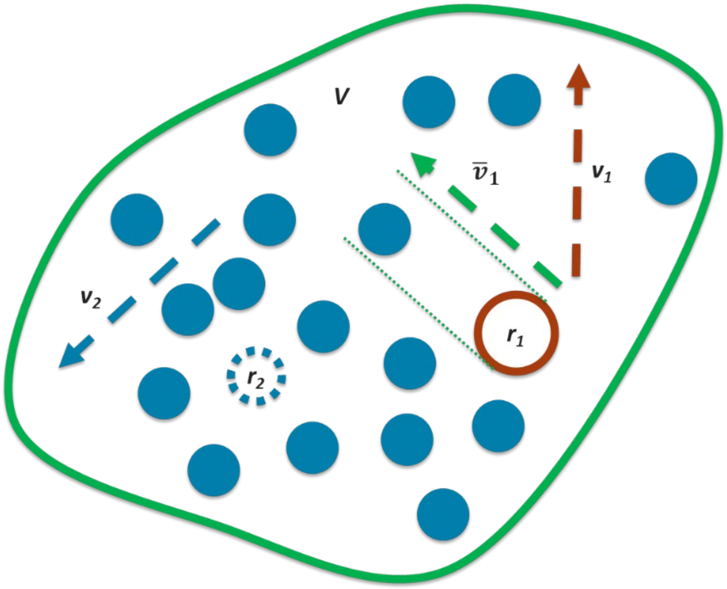

Figure 3. A schematic representation of the UC-UC collision calculation. The first particle, shown in red, travels at velocity $\bar{v}_1$ with respect to the blue particles over a time period of Δt, passing through a volume marked by the green dotted line. if one of the n particles, distributed randomly over the volume V, crosses paths with the first, a collision can be said to have occurred.

Interactions between the UC particles and the crucible wall were also considered. Two possibilities were considered. In the first, only 2% of the velocity was lost in the colliding direction, and in the second, 90% of velocity was lost in the colliding directing. The combination allows us to explore the effect of UC-UC interactions and UC-crucible interactions on the evolving distribution of UC particles within the melt. This also allows some exploration of the evolution of the UC particle size for the cases in which perfectly inelastic collisions are allowed. In each case, simulations were run for 900 seconds, which is approximately the amount of time U would be expected to remain at temperature. A list of simulation parameters and literature sources, when available, is shown in Table 1. Where no source is indicated, the value was determined experimentally or by computational design. In each simulation, the final positions and volumes of the UC particles were tabulated to quantify the associated effect on UC particle size and spatial distribution within the melt.

Table 1. Parameters used in particle collision simulations.

Parameter	**Description**	**Value (Units)**	**Source**
η	Viscosity	0.0065 Pa·s	[60]
r	UC Radius (μm)	0.5 μm	-
T	Temperature (K)	1403.15 K	-
V_f	UC Volume Fraction	1%	-
l	Cell Width	1 mm	-

3. Results and Discussion

3.1 Validation of the simulation framework

Preliminary flow simulations were conducted to validate the simulation framework and gauge the accuracy of the predicted flow field. As mentioned earlier, experimental data for the flow field and particle motion are not available for the current experimental setup with uranium. Therefore, we chose experimental data from the literature describing similar flow physics. Ščepanskis et al.[5, 46, 61] conducted experimental and numerical studies to investigate the flow field and particle transport in Wood's alloy melt (50%Bi –26.7%Pb –13.3%Sn –10%Cd, eutectic, melting point 70°C) in an induction furnace.[61] Ščepanskis et al.[61] used a glass crucible in their experiment whose size and EM parameters corresponded to ICF2 in this report (Figure 4). In their equipment, 1.3 kW of power corresponding to 432 Amperes was used. This power led to a heating rate of 1.8°C/s, limiting the maximal duration of the experiment, since temperatures above 150°C lead to release of toxic compounds from the experimental setup. Solid spherical particles were put on the top surface of the melt to study the mixing process and deposition of inclusions on the crucible wall. Details of the parameters involved in the flow simulations are provided in Appendix D.

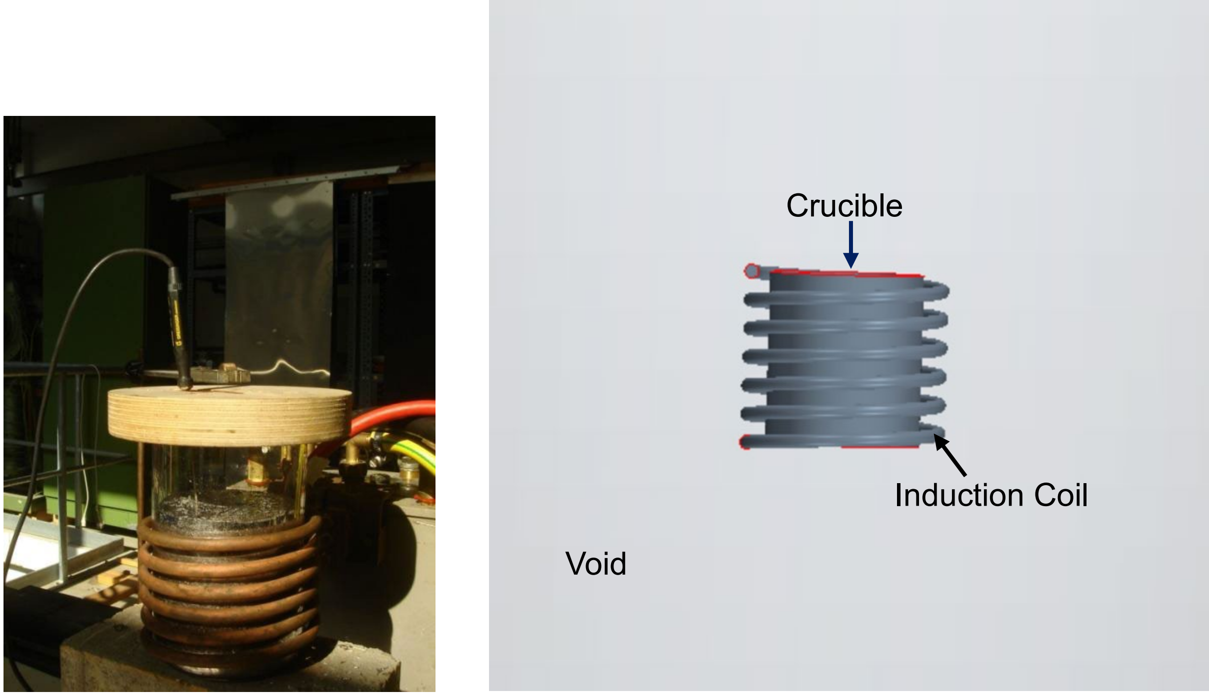

(a) (b)

Figure 4. (a) Experimental setup used by Ščepanskis[61] shows the copper induction coil with six turns surrounding a glass crucible of Wood's metal. (b) Computational flow domain reported here to reproduce the Wood's metal system.

In our study, a computational flow domain matching the Ščepanskis experimental setup was developed with STAR-CCM+. In addition to the crucible and induction coil, the flow domain has a large surrounding void to model the electromagnetic fields, as required for appropriate resolution of the boundary conditions of the magnetic field. In the void region, physical properties such as electrical conductivity, density, magnetic permeability, etc., of the air was specified (see Appendix D).

Next, the computational flow domain was meshed in STAR-CCM+. A nonuniform meshing scheme was used to accurately capture the physics. The flow region proximate to the crucible/melt/induction coil was meshed with a fine mesh (see Figure 5). Near the crucible wall an induction coil, boundary layer meshing was used. Note that the Lorentz force density in a thin layer near the wall was found to be very high. Therefore, a very fine and dense mesh was required there to capture the physics. In the current setup of the induction furnace, the Lorentz force is the driving force for stirring process.

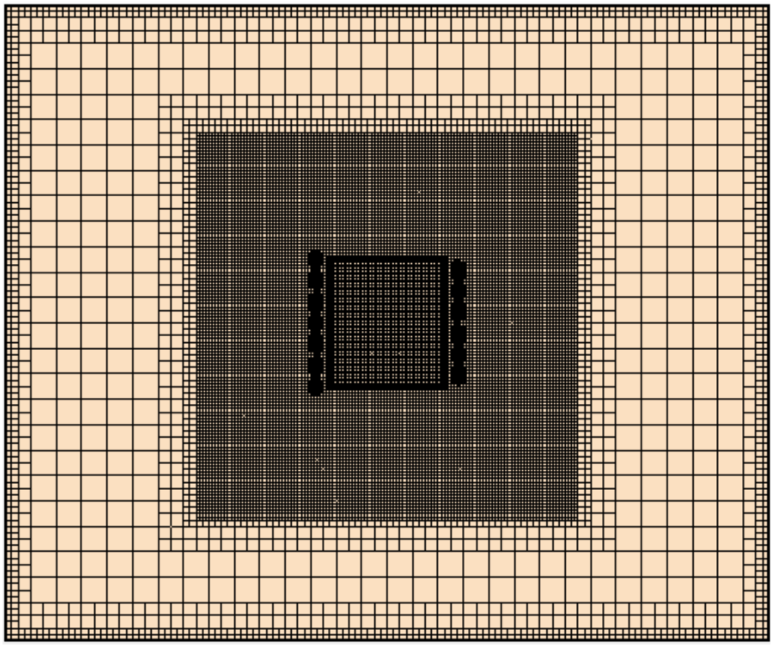

Figure 5. Meshing scheme used in the discretization of the computational flow domain. A very fine mesh was used in the region proximate to the crucible and induction coil.

After meshing, flow simulations were conducted with the parameters specified in Appendix D for ICF2. The simulations for computation of the Lorentz force using electromagnetic induction were conducted until the Lorentz force reached a steady value. As seen in Figure 6, the maximum value of the Lorentz force exists in the region proximate to the crucible wall. Simulations using FEMM and STAR-CCM+ show a similar maximum values of the Lorentz force density (5e+05 N/m^3).

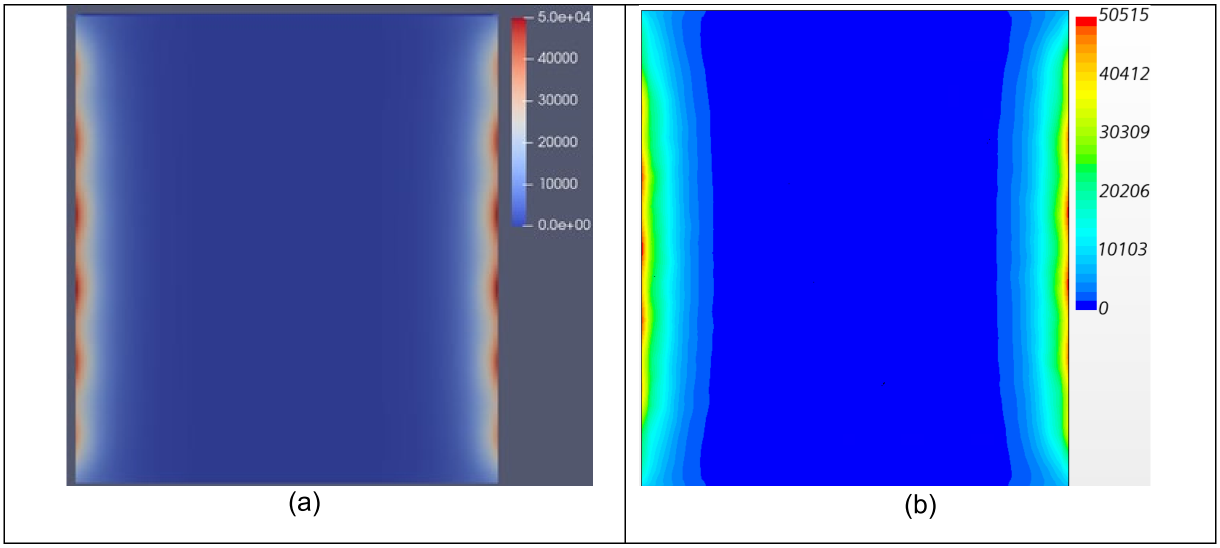

Figure 6. Lorentz force distribution at the XZ plane of the ICF2 obtained from (a) the FEMM simulation and (b) the STAR-CCM+ simulation.

Ščepanskis *et al.*[5] showed the radial variation of the Lorentz force density in the case of oxide particles (non-conductive and non-magnetic). However, the value of radial variation of the Lorentz force in the melt was not presented. It is assumed that the Lorentz force on the oxide particle will be close to that existing in the melt. This assumption could lead to some discrepancy in the comparison of the Lorentz force. Figure 7 compares the variation of the radial component of the Lorentz force density at three vertical locations in the melt. The Lorentz force exponentially decays from the crucible wall to center of the melt. Ščepanskis shows slightly higher values whereas the Lorentz force predicted by STAR-CCM+ and OpenFOAM simulations are nearly identical.

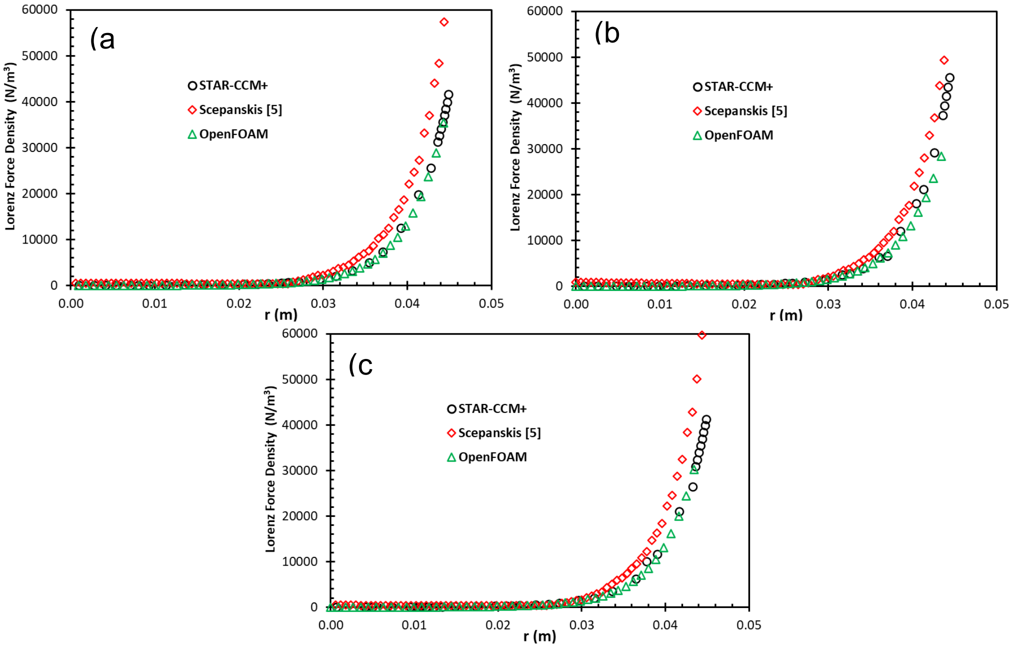

Figure 7. Comparison of the magnitude of the Lorentz force density (radial component) at three heights in ICF2: (a) 7cm, (b) 5cm and (c) 3 cm from the bottom of the crucible.

Next, the Lorentz force computed from the simulation was exported and used as an additional momentum source term in the flow simulations. The transient flow simulations were conducted with adaptive time steps, keeping the Courant number below 0.5. The time averaged velocity field is presented in Figure 8. The velocity vector in the right half of the X-Z or vertical plane is shown, similar to Ščepanskis' work. Note that the four rotating vortices (2 when the crucible representation is bisected vertically) appear in the flow domain. The centers of the vortices is near the crucible wall. The vortices push the flow toward the wall at the top and bottom of the crucible, while in the middle, they push the flow away from the wall, giving rise to a velocity maximum near the wall. The time averaged velocity field computed in both simulation frameworks matches well with independent flow simulations by Ščepanskis,[5] both qualitatively and quantitatively.

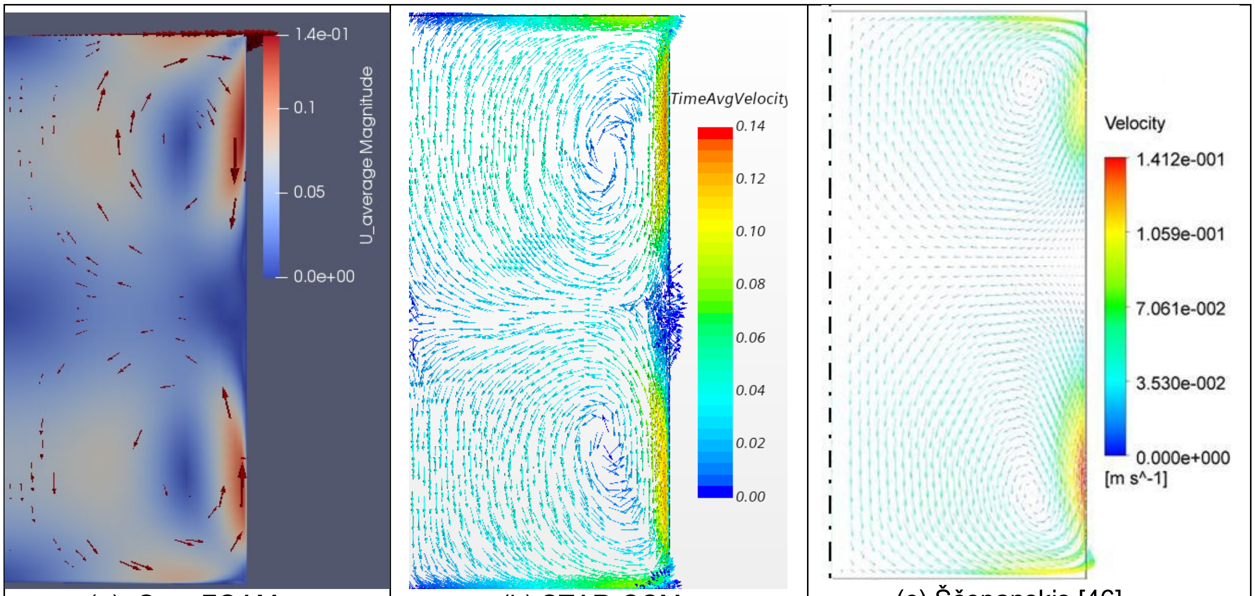

(a) OpenFOAM

(b) STAR-CCM+

(c) Ščepanskis [46]

Figure 8. Velocity field distribution at the X-Z plane of teh ICF2 from (a) OpenFOAM, (b) STAR-CCM+ and (c) Ščepanskis.[46]

After successful validation of the flow field, flow simulations were further extended to investigate the particle/inclusion motion and depositions in the melt. The Lagrangian tracking scheme was used to simulate the particle motion. The time averaged velocity field was used to track the inclusion trajectories. Consistent with the experimental and numerical studies by Ščepanskis,[5] approximately 84,000 spherical particles with diameters pf 400 microns were injected from the top of the melt. As mentioned, the inclusions are non-magnetic and non-conductive. Therefore, magnetic and electrical forces acting on the particle were not considered. The transient flow simulations were continued until a quasi-steady state was reached. The interacting turbulent vortices prevent the system from evolving to a true steady state, and more work-up of particle motion simulation outputs for comparison with the literature is required. Since systematic flow simulations conducted in both custom frameworks reported here matched well with independent simulation data from the literature in terms of radial Lorentz force and velocity field, it was concluded that the simulation frameworks developed in the current investigation are validated and can be further used in other similar flow models.

3.2 Velocity Field in the Lab/Uranium case

After successful validation, the simulation frameworks were deployed to investigate the migration of UC in the induction furnace with U. As in previous studies, the Lorentz force was computed first, followed by the flow field inside the U melt and finally the trajectory of the UC in the U melt. The details of the dimensions and design of the induction furnace at the RPL are presented in the Appendix D. As mentioned earlier, the meshing of the flow domain was conducted in STAR-CCM+. Figure 9 (left) shows the experimental setup at the RPL. Based on corresponding experimental physical parameters, the computational flow domain was developed. Similar to preliminary studies described above, the computational flow domain was meshed with a non-uniform mesh. A fairly coarse mesh was used in the void region away from the crucible and induction coils (see Figure 10).

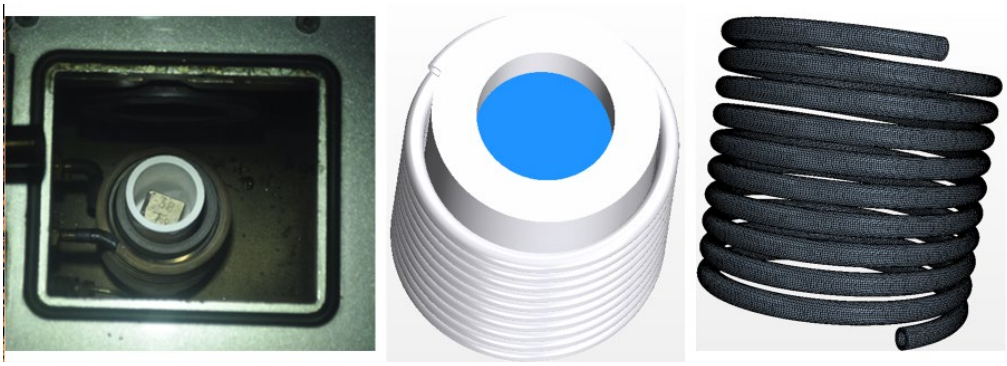

Figure 9. (Left) Experimental setup and corresponding (middle) simulation setup used in the investigation. The blue region shows the melt in the crucible. (Right) Model of the induction hollow wired coil used in the simulations.

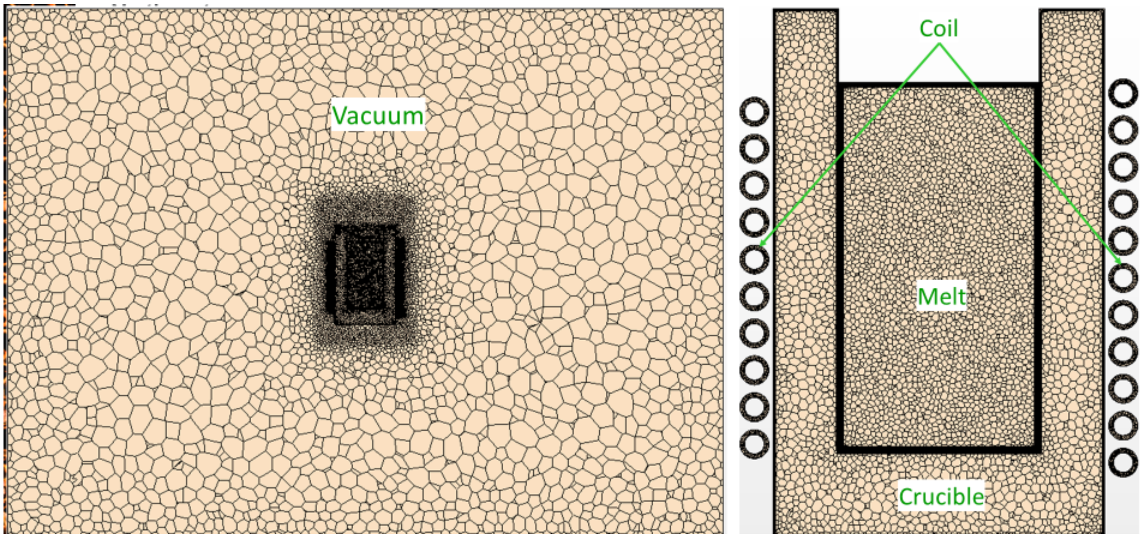

Figure 10. (Left) Meshing scheme used in the discretization of the computational flow domain of the Lab/Uranium setup. (Right) Exploded view at the center shows a very fine mesh was used in the region proximate to the crucible and induction coil.

After meshing, flow simulations were conducted with the set of parameters described in Appendix D. An alternating current of 450 A with a frequency of 15 kHz was used in the induction coil. This current was sufficient to achieve the melt temperature of 1400°C. The physical properties of the melt at that temperature were used in the flow simulation. The experimental values for the velocity field and Lorentz force were not experimentally available. Therefore, results were only compared between the two simulation frameworks. The Lorentz force and velocity field matched well. Figure 11 shows a maximum Lorentz force value of 3.4e+05 N/m^3 was found in the vicinity of the crucible wall. Figure 12 shows the time averaged value of the velocity vector field. In this case, the locations of the vortices are not symmetric about the midpoint horizonal axis of the melt. This is due to the off-center position of the induction coil that drives the flow. The velocity field obtained from the simulations was further used in the investigation of the migration of the UC inclusions.

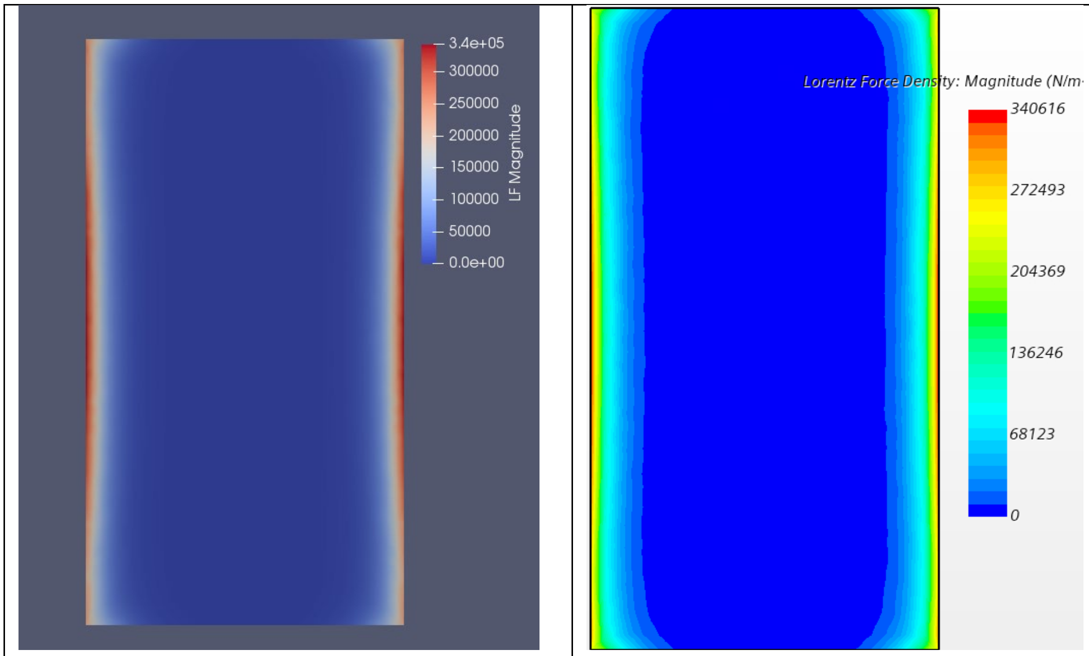

FEMM Lorentz force for Lab/Uranium case

Star-CCM+ Lorentz force for Lab/Uranium case

Figure 11. Lorentz force for the Lab/Uranium case. Units given in N/m^3.

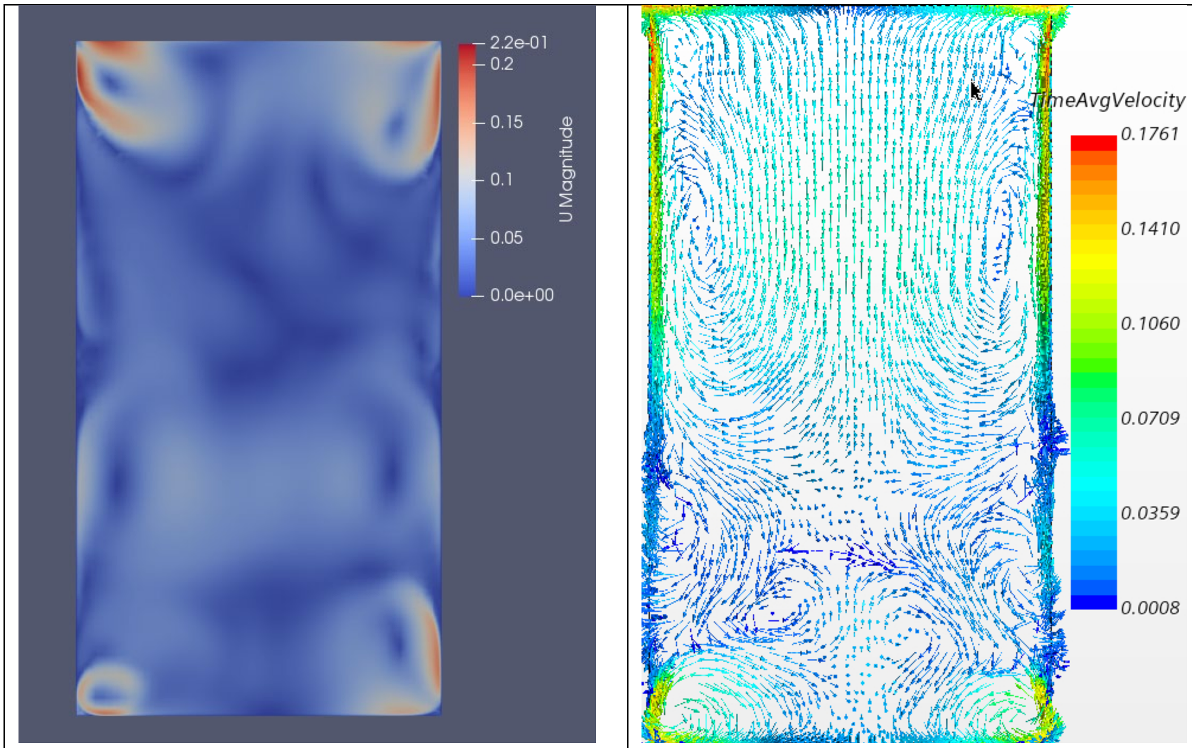

(a) OpenFOAM

(b) STAR-CCM+

Figure 12. Velocity fields for the Lab/Uranium case. Units are given in m/s.

The particle distribution in the Lab/Uranium case is shown in Figure 13 for 1 μm particles. First, a steady state flow was developed, and then particles were introduced uniformly in the melt. Particles were again tracked long enough for a steady state to be obtained. This distribution seems reasonable, given that the particles are lighter than the melt and tend to rise to the top.

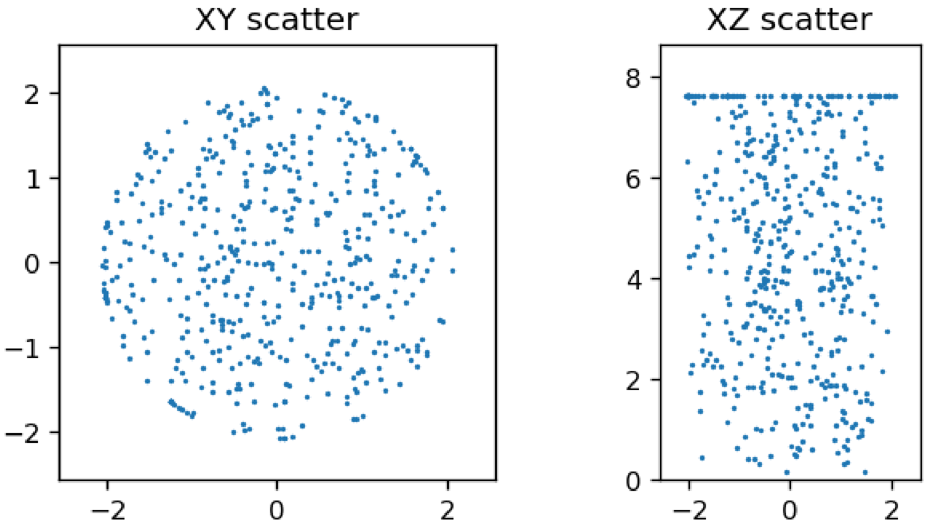

Figure 13. Simulated projections of particle positions in the cylindrical crucible generated from OpenFOAM.

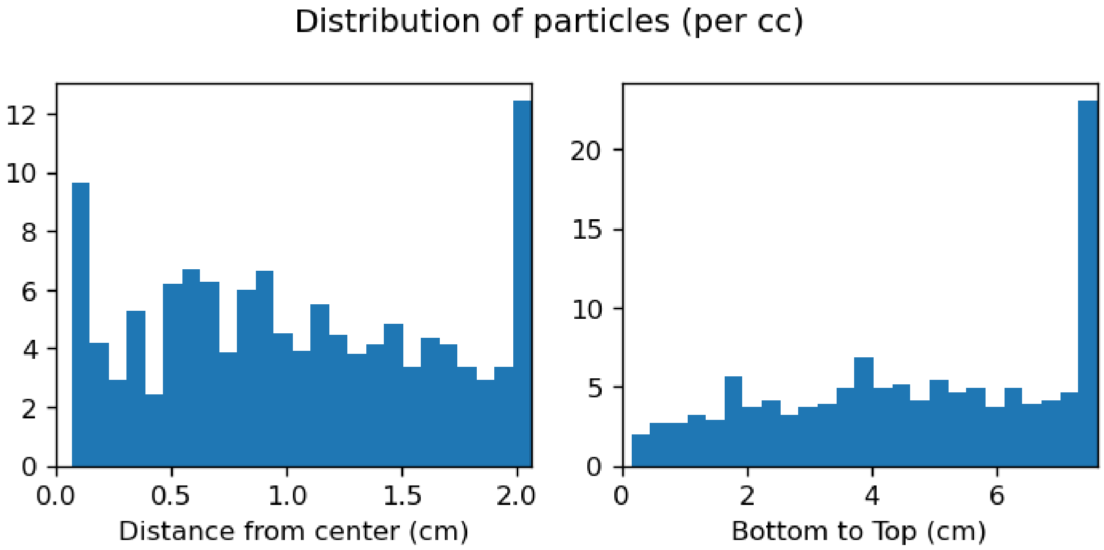

Figure 14. Particle distribution in simulated U melt from OpenFOAM.

3.3 FPKMC particle tracking

3.3.1 Effect of UC-Crucible Interaction

Simulations of collisions between UC particles and the crucible walls show that the UC-wall interaction can greatly affect the spatial distribution of UC particles in the U melt pool. As shown in Figure 15, UC particles tend to collect near the crucible walls when these collisions greatly reduce the UC velocity. The UC particles also accumulate near the top of the melt pool due to the influence of the buoyant force. However, when these collisions only slightly reduce UC velocity, the UC particles are much more evenly distributed within the melt.

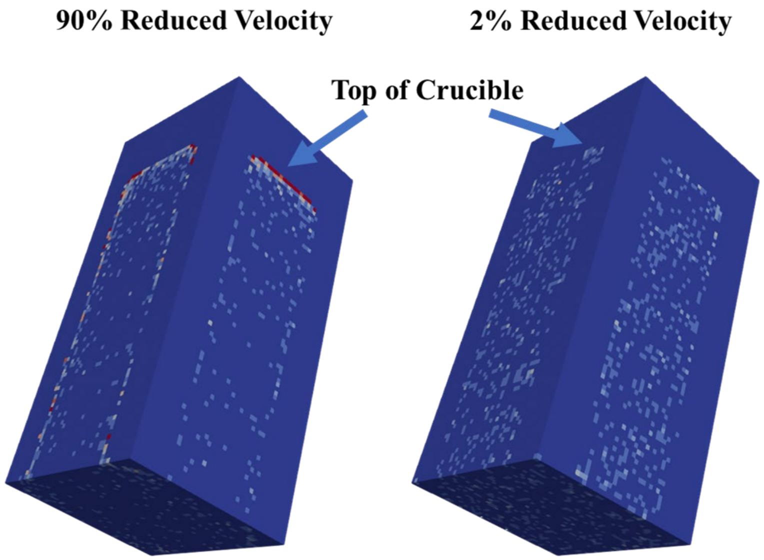

Figure 15. The distribution of UC particles within the U melt pool for cases in which UC-wall collisions reduce UC velocity by 90% (left) and 2% (right).

As will be shown, this effect is relatively consistent regardless of the UC-UC interaction and the present velocity field.

3.3.2 Effect of UC-UC Interaction

The interaction between UC particles visually has a smaller effect on the spatial distribution of UC particles, as shown in Figure 16. The spatial distribution, as affected by the UC-crucible interaction is essentially the same, with UC particles accumulating near the crucible walls when collisions significantly reduce particle velocity and remaining well distributed within the melt when the loss of particle velocity is small. However, it is also clear that collisions between UC particles in the case of perfectly inelastic UC-UC collisions results in particles that have significantly agglomerated. The effect of the UC-crucible interaction, as well as the molten U velocity field on the agglomeration of the UC particles, is shown in Figure 17. These plots show that the molten U velocity field and the UC-crucible interaction compete in their effects on UC agglomeration. The UC-crucible interaction visibly suppresses UC agglomeration when UC particles lose considerable velocity during collisions. In these cases, a period of agglomeration is observed, followed by a period in which growth stagnates. This is apparently caused by the fact that more UC migrates towards the crucible walls, where it moves more slowly. Collisions, in this case, become less frequent. However, depending on the velocity field created by induction heating, additional agglomeration can be achieved. Even when 90% of velocity is lost in UC-crucible collisions, significantly more agglomeration is observable when simulations assume the middle or late U velocity field in terms of time of induction stirring as opposed to the early U velocity field.

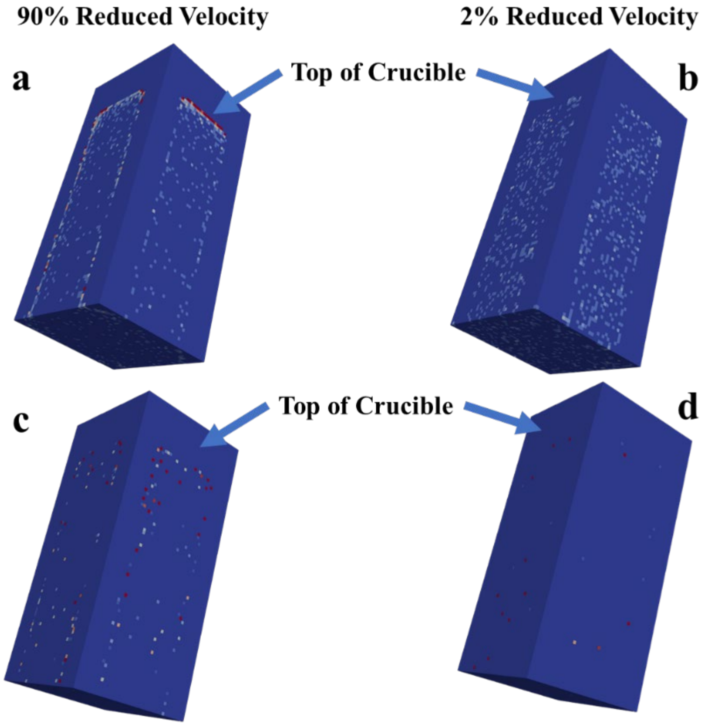

Figure 16. The spatial distribution of UC particles, given cases in which UC particles do not interact and UC-crucible collisions reduce velocity by 90% (a) and 2% (b), and cases in which UC particles collide inelastically for UC-crucible collisions which reduce velocity by 90% (c) and 2% (d).

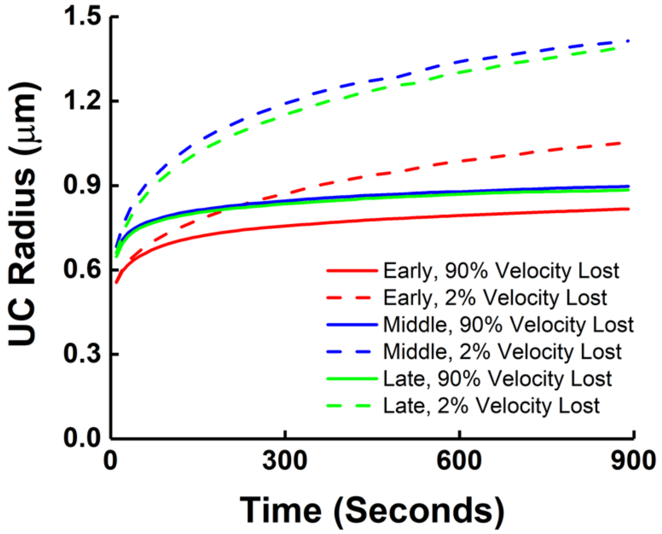

Figure 17. The change in UC particle average radius over 900 seconds for cases of inelastic UC-UC collisions, as affected by the UC-crucible interaction and the molten velocity field.

The effect of the velocity field increases when the UC-crucible collisions have a smaller effect on UC velocity. When only 2% of velocity is lost in collisions, the middle and late velocity fields (in terms of time of induction stirring) achieve an average radius of over 1.2 microns, while only an average of approximately 0.75 microns is achieved when using the early velocity field.

3.3.3 Effect of Velocity Field

While the molten U velocity field has a significant effect on UC agglomeration, it does not have any obvious effect on the spatial distribution of the UC particles, as shown in Figure 18. In these cases, we can see that when UC particles do not interact, the UC-crucible interaction has a strong influence on the spatial distribution of the carbides.

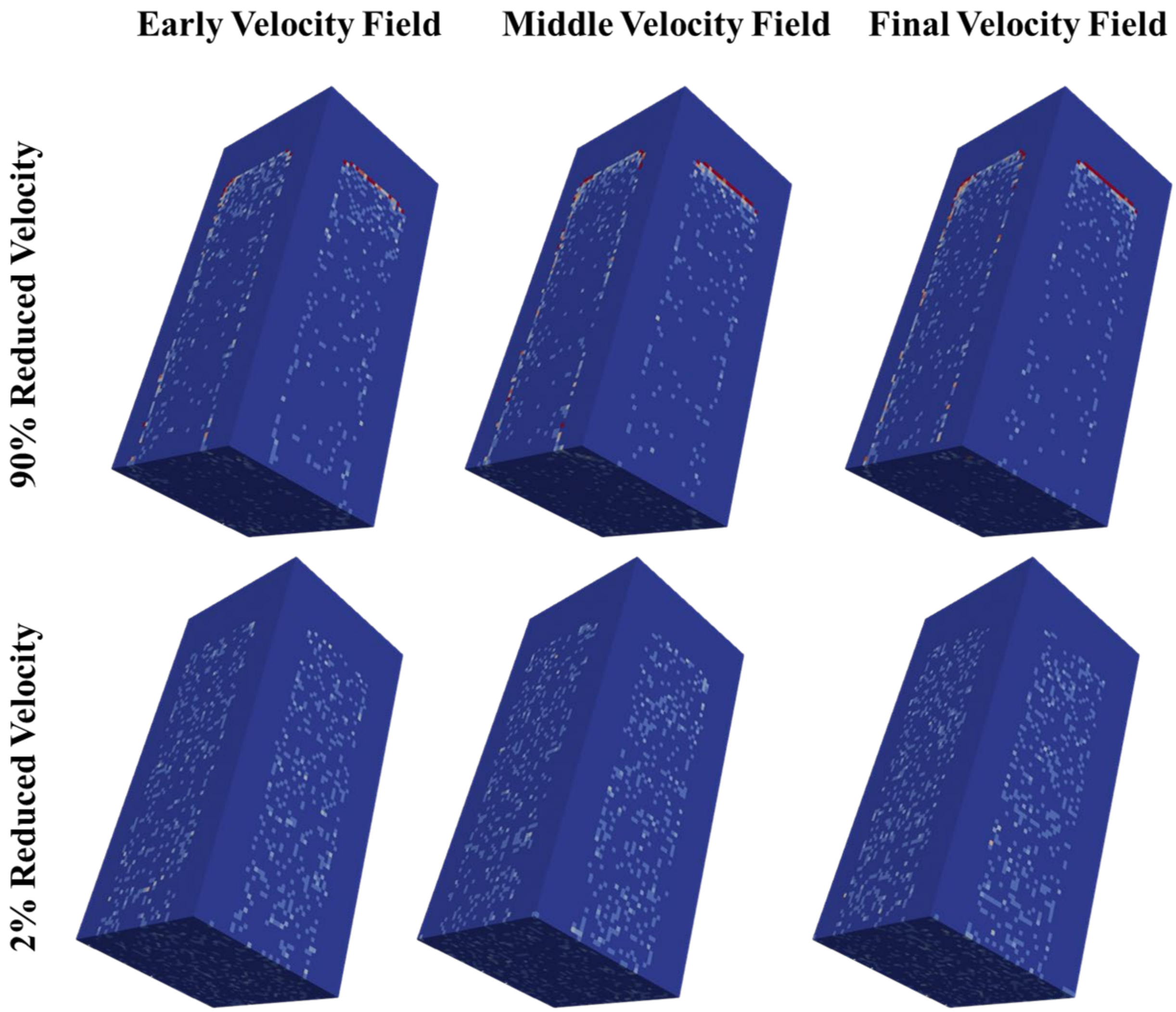

Figure 18. The spatial distribution of UC particles, given cases in which different velocity fields are used based on initiation of induction mixing, assuming either 90% of velocity of 2% of velocity is lost in collisions between the UC particles and the crucible walls. In the cases shown, it is assumed that UC particles do not interact. Red indicates areas of high particle density.

We inspected this trend more closely through an analysis of the fraction of UC particles accumulated within 1 mm of the crucible walls, shown in Figure 19. We show that the velocity field has a minor effect on the fraction of the UC particles that end up near the crucible wall. For example, we can see that when 90% of velocity is lost upon UC-crucible collisions, the fraction of UC present on the crucible walls is generally lower for the early velocity field than the middle and late velocity fields. This trend reverses when only 2% of velocity is lost. Instead, generally more UC particles accumulate near the crucible walls in these cases. The cause for this effect is not immediately clear. The UC-UC interactions themselves appear to have a greater effect on the UC accumulation than the molten U velocity field. The UC-crucible interaction is by far the strongest influencing factor. When 2% of velocity is lost in UC-crucible collisions, roughly half as many as UC particles migrate to the edge of the melt pool near the crucible as when 90% of velocity is lost.

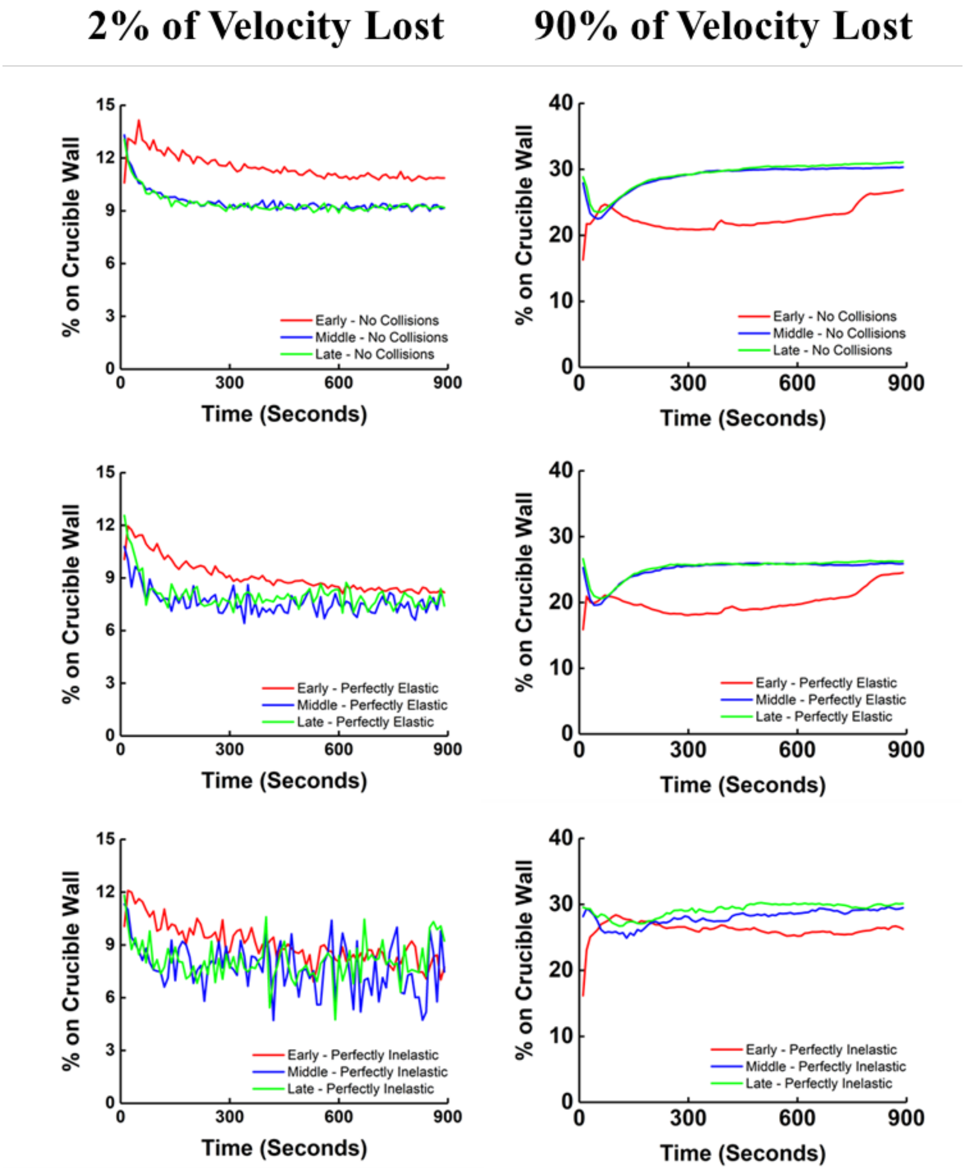

Figure 19. The fraction of UC particles present within 1 mm of the crucible wall, as a function of the UC-UC interaction, the UC-crucible wall interaction, and the three velocity fields simulated.

Histograms of the positions of the particles in three different cases after 900 s generated using the FPKMC apprach, shown below in Figure 20, confirm that this general behavior is prevalent in a manner similar to that predicted for OpenFOAM and Star-CCM+ models, as described in the following section.

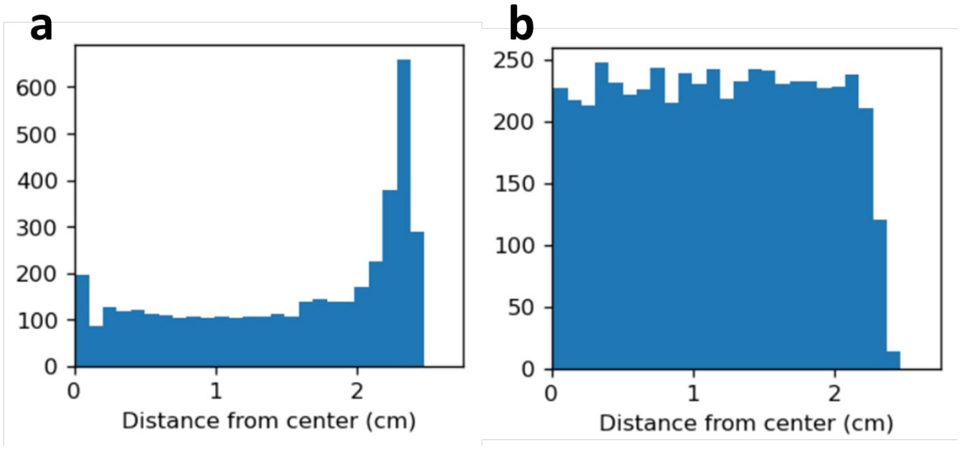

Figure 20. A histogram of the distribution of UC particles present within the melt after 900s, assuming the middle velocity field and no UC-UC interaction, as a function of distance from the central axis. For these simulations we assume either 90% of velocity is lost upon UC-wall collisions(a) or 2% of velocity is lost upon UC-wall collision (b).

3.4 OpenFOAM and Star-CCM+ particle tracking

Particle tracking studies were also performed using Star-CCM+ and OpenFOAM. The computed velocity field in the flow simulation was used in the calculation of UC migration in the uranium melt. Similar to the preliminary studies for validation of the simulation framework, 27,500 spherical particles with micron sizes were injected in the flow domain. Based on the number of particles and size, the volume fraction of the particle was found to be extremely low and falls under the extremely dilute regime. Based on that, one-way coupling was used in the flow-particle simulations, so that only the continuous phase (the melt) exerts a force on the discrete phase (UC impurities), but there is no effect from the particles on the flow. Systematic simulations were conducted to investigate the effect of particle size on the UC migration phenomenon. As expected, a uniform distribution of the particles in the vertical and horizontal directions is seen at smaller sizes (1 and 10 microns) in Figure 21 and Figure 22. At larger sizes, particle inertia and a higher buoyancy force lead to the particle movement toward the wall and to the top of the melt (see Figure 21 and 22).

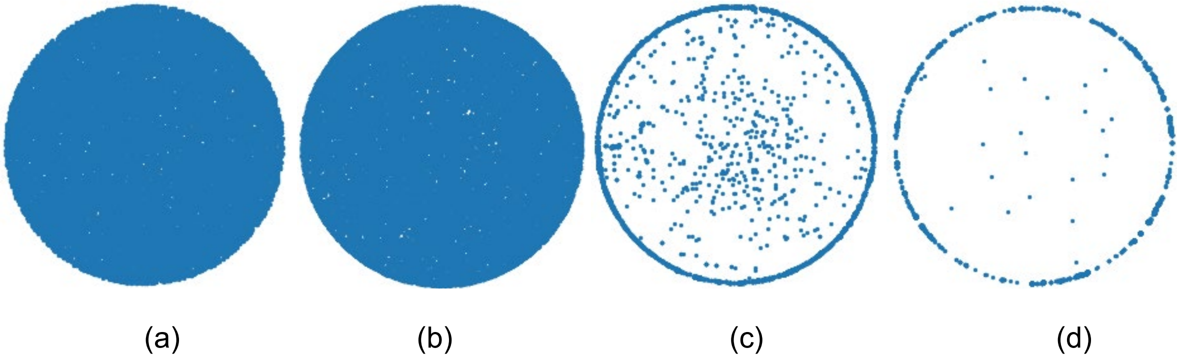

Figure 21. Top view (X-Y plane) of particle distributions in the crucible. Particle size in the picture is not drawn to scale and is instead shown in the pixel scale for better visibility. (a) 1 micron, (b) 10 microns, (c) 50 microns and (d) 100 microns.

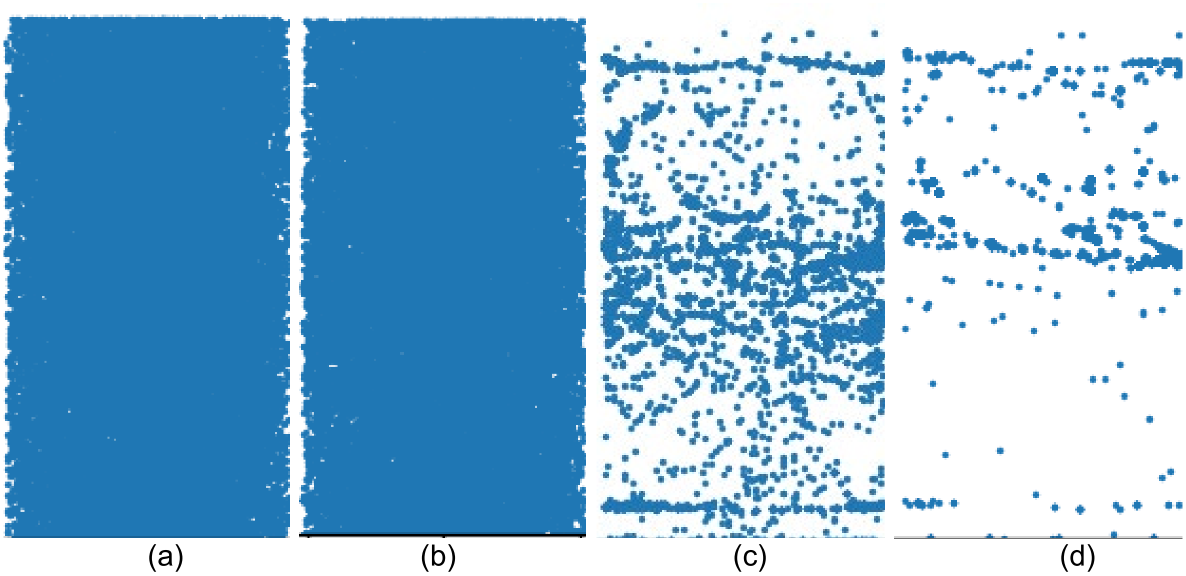
(a) (b) (c) (d)

Figure 22. Front view (XZ plane) of the particle distributions in the crucible. Particle size in the picture is not drawn to scale and is instead shown in the pixel scale for better visibility. (a) 1 micron, (b) 10 microns, (c) 50 microns and (d) 100 microns.

The particle migration behavior was further quantified and analyzed in terms of histogram plots (Figure 23). The histogram plots show similar behavior. A uniform particle distribution was observed at lower particle sizes.

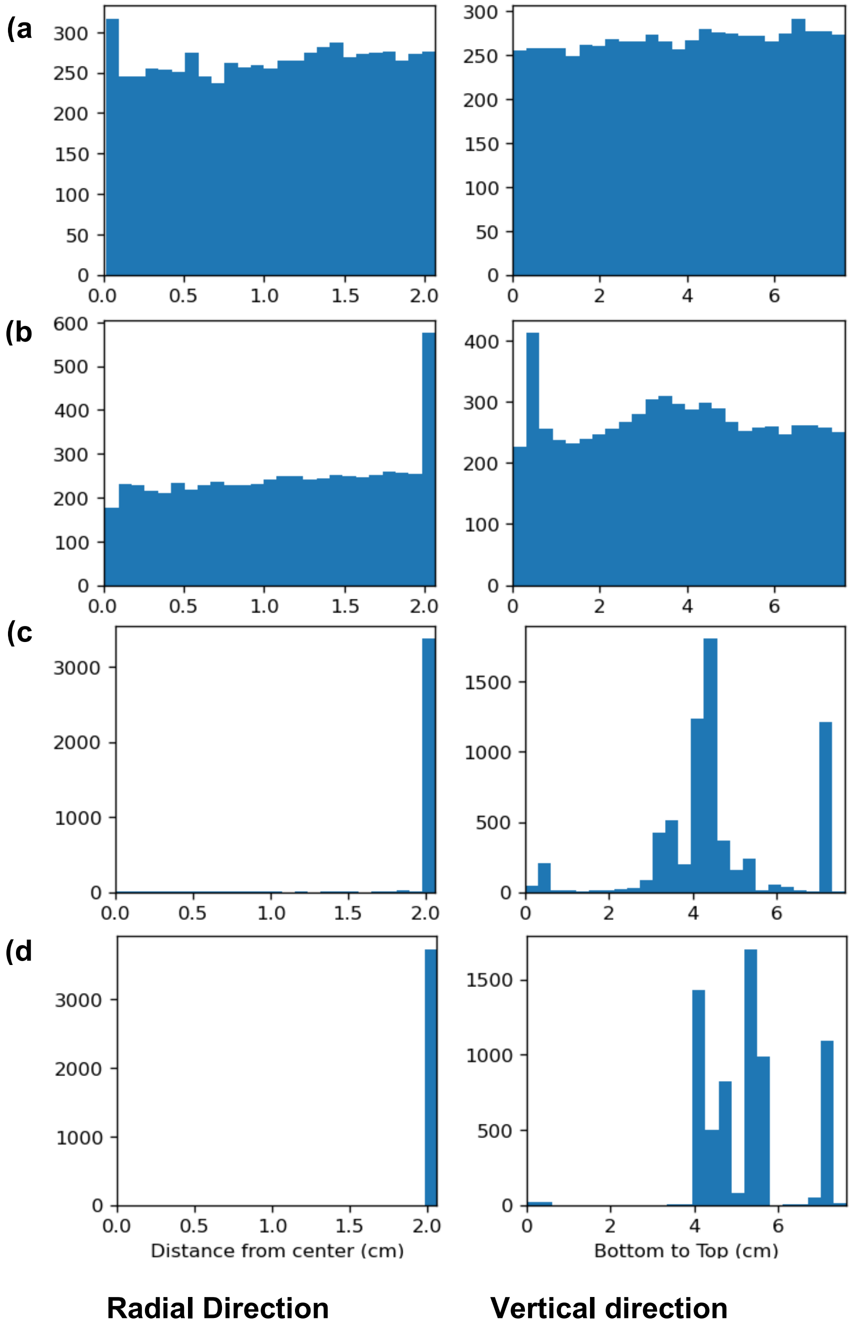

Figure 23. Effect of the particle size on in the radial (Left) and vertical (Right) distributions of particles in the crucible. (a) 1 micron, (b) 10 microns, (c) 50 microns and (d) 100 microns.

4. Conclusion

Impurities and microstructure formation play a critical role in the overall physical properties and performance of the final metal product. Understanding the impurities and their migration can lead to improved material properties. In this context, computational fluid dynamics models for particle-flow simulation in an induction furnace have been developed to investigate the migration of carbon impurities in molten uranium during the casting process. Independent results from STAR-CCM+ and FEMM for electromagnetic force (Lorentz force density) were found to match quite well. The predicted value of velocity fields using OpenFOAM and STAR-CCM+ matched well with the predictions by Ščepanskis *et al*.[5] Particle simulations were run using OpenFOAM, STAR-CCM+ and in house FPKMC code. The FPKMC code was also used to study particle agglomeration. Effect of particle size on the particle migration was also studied. At lower particle size (≤5 μm), homogeneous distribution of the particles in the molten metal was observed. With increased particle size, body force dominates, leading to clustering of particles near the wall. In addition, most particles stay in the upper half of the crucible, which is expected. For future work, it would be helpful to have experimental data on velocity fields and particle distribution within the U melt. This would help to increase confidence in the developed models. In summary, we have shown that open-source software can be used to model the migration of particles in an ICF.

5. References

[1] R. G. Surbella, M. T. Athon, Z. F. Huber and I. J. Schwerdt, *On direct carbon-monoxide inoculation of molten uranium: A potential strategy for developing working reference materials*, **2020**, Pacific Northwest National Laboratory, Richland, WA, PNNL-30273.

[2] N. L. Lahaye, M. T. Athon, Z. F. Huber, I. J. Schwerdt, R. G. Surbella, S. R. Adami, F. D. Heller, A. B. Luttman, L. E. Smith, D. E. Burkes and W. K. Pitts, *Experimental results for carbon monoxide inoculation of depleted uranium*, **2020**, Pacific Northwest National Laboratory, Richland, WA, PNNL-30272.

[3] M. J. Olszta, J. F. Corbey, M. T. Athon, Z. F. Huber, D. D. Reilly and D. G. Abrecht, *J. Alloys Compd.* **2022**, *Submitted*.

[4] M. J. Olszta, J. F. Corbey and D. D. Reilly, *J. Alloys Compd.* **2022**, *Submitted*.

[5] M. Ščepanskis, A. Jakovičs, E. Baake and B. Nacke, *Int. J. Multiphase Flow* **2014**, *64*, 19-27.

[6] A. Mazahery and M. O. Shabani, *Powder Technol.* **2012**, *217*, 558-565.

[7] J. M. Torralba, C. E. Da Costa and F. Velasco, *J. Mater. Process. Technol.* **2003**, *133*, 203-206.

[8] J. J. Stobbs and I. Whittle, *J. Nucl. Mater.* **1966**, *19*, 160-168.

[9] S. Zalkind, O. Sabag, I. Makover and S. Haroush, *J. Mater. Sci. Lett.* **2002**, *21*, 551-553.

[10] J. F. R. Ambler and G. F. Slattery, **1961**.

[11] A. a. T. Bauer, C.R. ; Farkas, M.S., *Microstructural studies of cast uranium*, **1965**, Country unknown/Code not available,

[12] D. M. Cheney and R. F. Dickerson, *Characterization of inclusions in dingot uranium*, **1957**, Country unknown/Code not available,

[13] R. F. Dickerson, A. F. Gerds and D. A. Vaughan, *JOM* **1956**, *8*, 456-460.

[14] P. E. Evans and T. J. Davies, *Journal of Nuclear Materials* **1963**, *10*, 43-55.

[15] B. R. T. Frost, *J. Nucl. Mater.* **1963**, *10*, 265-300.

[16] J. K. Ghosh and D. Vollath, *Metallography of uranium carbides and uranium-plutonium mixed carbides*, **1974**, Germany,

[17] H. A. Saller, *The identifcation of nonmetallic inclusions in commercial uranium*, **1955**, Battelle, Proceedings of the Metallurgy Information Meeting Held at Oak Ridge,

[18] G. L. Kehl and E. Mendel, *A study of inclusions in uranium. Final report*, **1963**, United States,

[19] G. A. Meerson, R. B. Kotel'nikov and S. N. Bashlykov, *The Soviet Journal of Atomic Energy* **1961**, *9*, 927-931.

[20] R. E. Rundle, N. C. Baenziger, A. S. Wilson and R. A. Mcdonald, *Journal of the American Chemical Society* **1948**, *70*, 99-105.

[21] C. A. Smith and F. Rough, *Nuclear Science and Engineering* **1959**, *6*, 391-395.

[22] H. E. Fairman and A. Kelly, in *Metallography and microstructures, 9*, (G. F. Vander Voort), ASM International, **2004**, 0.

[23] R. J. Jackson, *Vacuum-induction melting, refining, and casting of uranium and its alloys*, **1989**, ; Rockwell International Corp., Golden, CO (USA). Rocky Flats Plant, RFP-4186; Other: ON: DE90005522 United States 10.2172/5251555 Other: ON: DE90005522 NTIS, PC A03/MF A01 - OSTI; GPO Dep. HEDB English.

[24] C. T. Olofson, G. E. Meyer and A. L. Hoffmanner, *Processing and applications of depleted uranium alloy products*, **1976**, Battelle, Columbus, Ohio, MCIC-76-28

[25] A. J. Ardell, *Metall. Trans. A* **1985**, *16*, 2131-2165.

[26] D. Broek, *Engineering Fracture Mechanics* **1973**, *5*, 55-66.

[27] D. M. Davies and J. W. Martin, *J. Nucl. Mater.* **1961**, *3*, 156-161.

[28] N. C. Jessen Jr., *Melting and casting uranium and uranium alloys*, **1982**, Oak Ridge Y-12 Plant, Oak Ridge, TN, Y/DV-213.

[29] D. M. R. Taplin and J. W. Martin, *Journal of Nuclear Materials* **1964**, *12*, 50-55.

[30] I. Grenthe, J. Drozdzynski, T. Fujino, E. C. Buck, T. E. Albrecht-Schmitt and S. F. Wolf, *Chapter 5: Uranium, 1*, Springer, The Netherlands, 2010, 577.

[31] H. M. Lee, *Diffusion studies in uranium carbide systems*, Imperial College of Science and Technology (London), **1965**.

[32] M. H. Cornett, *Metallogrpahy of uranium: Procedures adn standards; nlco-954*, **1966**, National Lead Company of Ohio, Cincinnati, OH,

[33] B. Blumenthal, *J. Nucl. Mater.* **1960**, *2*, 197-208.

[34] W. A. Althaus, M. M. Cook and R. J. Bieker, *A study of as-cast and heat-treated urnaium-uranium carbide alloys by optical and electron microscopy*, **1966**, Natioanl Lead Company of Ohio, Cincinnati, OH, NLCO-968.

[35] A. V. Kuznetsov, *Int. J. Heat Mass Transfer* **1997**, *40*, 2949-2961.

[36] D. Sun, S. R. Annapragada and S. V. Garimella, *Int. J. Heat Mass Transfer* **2009**, *52*, 2966-2978.

[37] P. Doron, D. Granica and D. Barnea, *Int. J. Multiphase Flow* **1987**, *13*, 535-547.

[38] J. L. Bair, D. G. Abrecht, D. D. Reilly, M. T. Athon and J. F. Corbey, *J. Phys.: Condens. Matter* **2019**, *31*, 125901.

[39] C. Wang, A. Soulami, Z. Xu, G. Cheng, S. Hu, D. Burkes, W. E. Frazier, K. S. Choi, X. Wang, X. Hu, C. A. Lavender and V. V. Joshi, *Process modeling of u-10 wt% mo alloys using integrated computational materials engineering*, **2019**, Pacific Northwest National Laboratory, Richland, WA, PNNL-28640.

[40] W. Frazier, C. Wang, Z. Xu, N. Overman, S. Hu and V. V. Joshi, *Metallurgical and Materials Transactions A* **2020**, *51*, 533-544.

[41] K. E. Garrett, D. G. Abrecht, S. H. Kessler, N. J. Henson, R. Devanathan, J. M. Schwantes and D. D. Reilly, *Modelling and Simulation in Materials Science and Engineering* **2018**, *26*, 035013.

[42] M. Kirpo, A. Jakovics, E. Baake and B. Nacke, *Magnetohydrodynamics* **2007**, *43*, 161-173.

[43] A. Umbrashko, E. Baake, B. Nacke and A. Jakovics, *Metallurgical and Materials Transactions B* **2006**, *37*, 831-838.

[44] M. Kirpo, A. Jakovics, E. Baake and B. Nacke, *Magnetohydrodynamics* **2009**, *45*, 439-450.

[45] M. Ščepanskis, A. Jakovičs and B. Nacke, *Magnetohydrodynamics* **2010**, *46*, 413-423.

[46] M. Ščepanskis, A. Jakovičs and E. Baake, Journal of Physics: Conference Series, 2011,

[47] A. Asad, C. Kratzsch, S. Dudczig, C. G. Aneziris and R. Schwarze, *International Journal of Heat and Fluid Flow* **2016**, *62*, 299-312.

[48] M. Ščepanskis, A. Jakovičs, E. Baake and B. Nacke, *steel research international* **2015**, *86*, 169-174.

[49] E. Baake, S. Spitans and A. Jakovics, 2019 XXI International Conference Complex Systems: Control and Modeling Problems (CSCMP), 2019,

[50] F. Negrini, M. Fabbri, M. Zuccarini, E. Takeuchi and M. Tani, *Energy conversion and management* **2000**, *41*, 1687-1701.

[51] F. Hegewaldt, L. Buligins and A. Jakowitsch, *ELEKTROWARME INTERNATIONAL EDITION B* **1993**, *51*, B28-B28.

[52] S. Spitans, *Investigation of turbulent free surface flow of liquid metal in electromagnetic field*, Ph. D. thesis, University of Latvia **2015**.

[53] D. C. Meeker, 2018, Finite element method magnetics.

[54] T. Oppelstrup, V. V. Bulatov, A. Donev, M. H. Kalos, G. H. Gilmer and B. Sadigh, *Physical Review E* **2009**, *80*, 066701.

[55] W. E. Frazier, T. G. Lach and T. S. Byun, *Acta Materialia* **2020**, *194*, 1.
[56] A. Donev, V. V. Bulatov, T. Oppelstrup, G. H. Gilmer, B. Sadigh and M. H. Kalos, *J. Comput. Phys.* **2010**, *229*, 3214–3236.
[57] S. Elghobashi, *Applied Scientific Research* **1994**, *52*, 309-329.
[58] W. E. Frazier, S. Hu, N. Overman, C. Lavender and V. V. Joshi, *Journal of Nuclear Materials* **2018**, *498*, 254-258.
[59] W. E. Frazier, S. Hu, N. Overman, C. Lavender and V. V. Joshi, *Journal of Nuclear Materials* **2019**, *526*, 151763.
[60] D. Ofte, *Journal of Nuclear Materials* **1967**, *22*, 28-32.
[61] M. Ščepanskis, *The modelling of the behaviour of solid inclusions in the em induced recirculated turbulent flows of liquid metal*, University of Latvia (Rīga), **2014**.
[62] J. R. Nagel, *IEEE Antennas and Propagation Magazine* **2018**, *60*, 81-88.

Appendix A – FEMM Model and Outputs

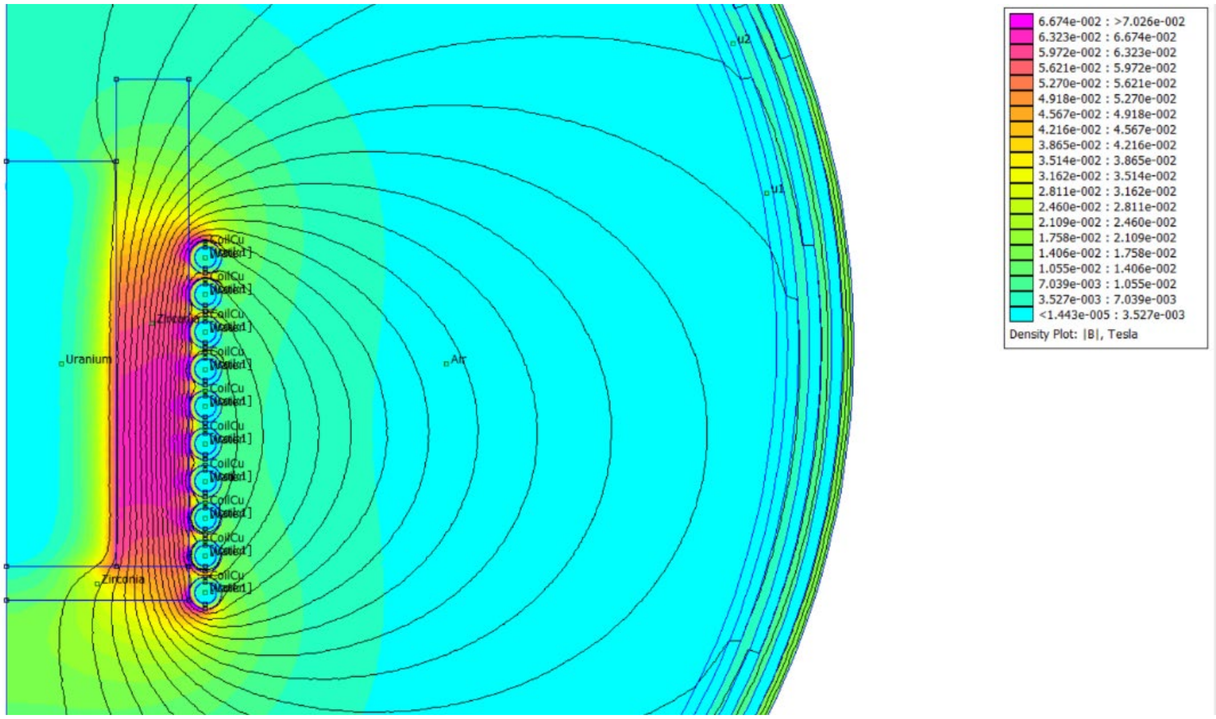

Figure 24. Illustration of FEMM model output showing magnetic field interaction with half the crucible, its contents, and the induction coil.

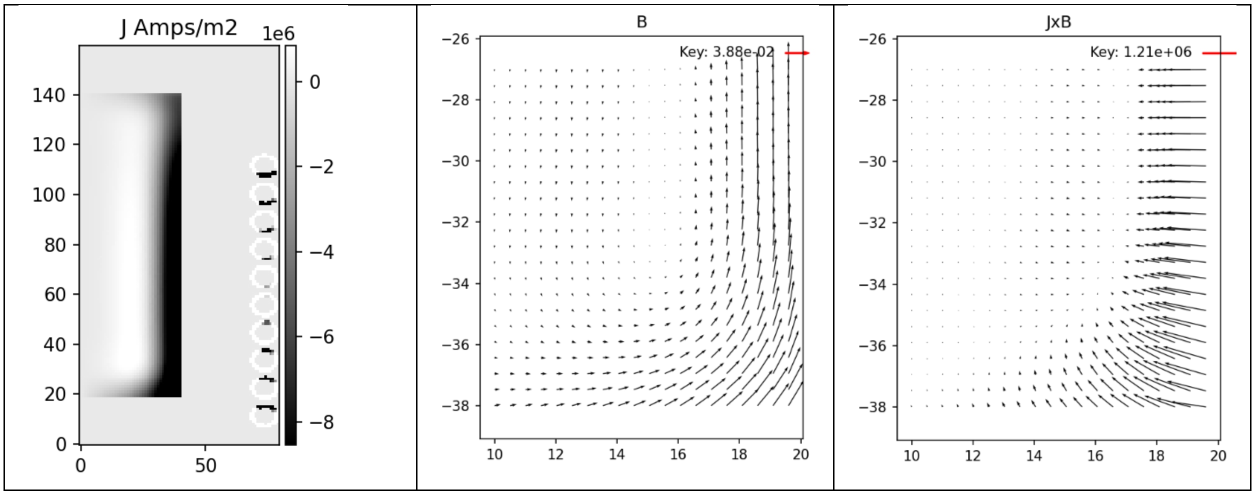

Figure 25. Show the J, B and JXB fields in the melt.

Appendix B – Check of FEMM Against Analytical Solution

The radial current distribution is given by: $J(r) = k\frac{B0}{\mu_0}\ \frac{J1(kr)}{J0(kr)}$,

where J0 and J1 are Bessel functions of the first kind with order zero and one.[62]

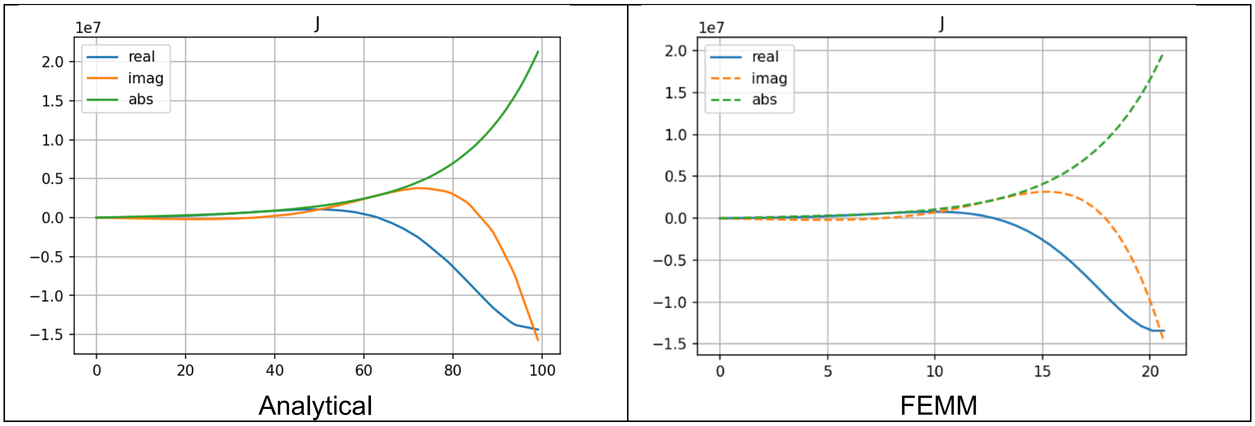

Analytical

FEMM

Figure 26. Induced current density in a cylinder obtained analytically (left) and numerically using FEMM (right)

Appendix C – Eddy Current Derivation

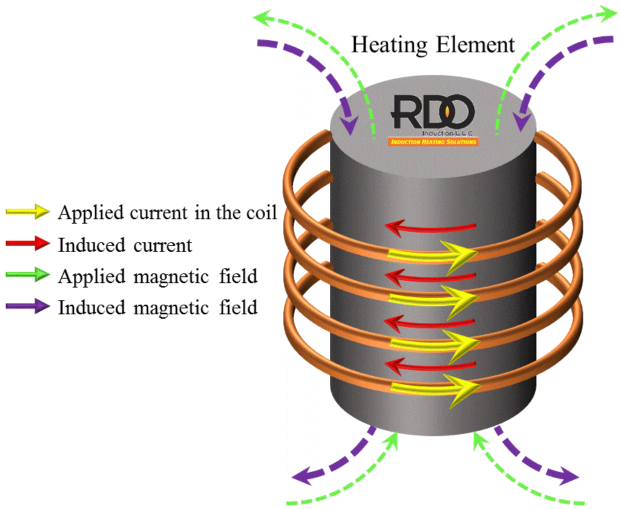

Figure 27. Rough illustration of direction of applied and induced currents. These are sinusoidal currents and can have a complex phase relationship with radial depth into the melt.

Subscript $_{app}$ is for applied quantities and are present over all space.

Subscript $_{ind}$ is for induced quantities and are present over all space.

Subscript $_{melt}$ is for quantities restricted to the melt. These are also induced quantities but restricted to the melt.

Consider an induction coil to which some current density J_{app} is applied, producing a magnetic field B_{app}.

If a piece of metal/melt is situated inside the coil, there will be induced EMF E_{ind} and induced current J_{melt} in the metal which will produce its own magnetic field B_{ind} such that:

$$\mathbf{B_{net}} = \mathbf{B_{app}} + \mathbf{B_{ind}}$$

B_{app}, B_{ind} exist both inside and outside the melt and equation 1 above is true for both inside and outside the metal.

Now consider the inside of the metal where applied current density is zero and only the induced current density J_{melt} exists. Here, Ampere's Law ($\nabla \times B = J$) says:

$$\nabla \times \mathbf{B_{app}} = 0$$

$$\nabla \times \mathbf{B_{ind}} = \mu_0 \, \mathbf{J_{melt}}$$

Note: B_{ind} is not restricted to the melt, but the curl of B_{ind} is restricted to melt.

Substituting Ohm's Law (J = σE, where σ is conductivity) we get:

$$\nabla \times \mathbf{B_{ind}} = \mu_0 \sigma \, \mathbf{E_{melt}}$$

Now we want to relate the electric field in the melt, E_{melt} to the change in magnetic flux that induces the $E_{melt.}$

Faraday's law says ∇xE = -dB/dt. Note that in the differential form it gives us the curl of E, not E.

So we take the curl of both sides of Eq. 4 and get:

$$\nabla \times \nabla \times \mathbf{B_{ind}} = \mu_0 \sigma \nabla \times \mathbf{E_{melt}}$$

Now that the RHS has curl of E, we can substitute from Faraday's law:

$$\nabla x \nabla x B_{ind} = -\mu_0 \sigma \frac{dB_{net}}{dt}$$

Note: E_{melt} is the result of the derivative of both induced and applied B)

$$\nabla \times \nabla \times \mathbf{B_{ind}} = -\mu_0 \sigma \left(\frac{dB_{app}}{dt} + \frac{d\mathbf{B_{ind}}}{dt} \right)$$

Applying the vector identity ∇ x ∇ x B = -∇^2B + ∇(∇.B) we get:

$$\nabla^2 \mathbf{B_{ind}} + \nabla(\nabla . \mathbf{B_{ind}}) = -\mu_0 \, \sigma \left(\frac{d\mathbf{B_{app}}}{dt} + \frac{dB_{ind}}{dt} \right)$$

Since ∇.B is always zero (no monopoles), this reduces to:

$$-\nabla^2 B_{ind} = -\mu_0 \, \sigma \left(\frac{dB_{app}}{dt} + \frac{dB_{ind}}{dt} \right)$$

Assuming B has a sinusoidal profile, dB/dt = jωB.

$$-\nabla^2 \mathbf{B_{ind}} = -\mu_0 \, \sigma \, (j\omega \mathbf{B_{app}} + j\omega \mathbf{B_{ind}})$$

This is the standard vector-Helmholtz equation with non-homogenous forcing function. It expresses the causal relationship between an applied magnetic field B_{app} and the induced field $B_{ind.}$

Once B_{ind} is obtained over the melt, J_{ind} in the melt can be found using Ampere's law.

Once J_{ind} is known over the melt, Joule heating in the melt can be obtained using $J.J^*$ (J and B are complex quantities or phasors)

The Lorentz force can be obtained using: $\mathbf{F} = \mathbf{J} \times \mathbf{B}$.

Some points about calculating the Lorentz Force:

J and B are complex quantities, and the computation of the cross product involves two phasor multiplications.

Phasors can only represent a single frequency. The product of two sinusoids at fq. ω is a sinusoid at fq. 2ω. Naïve phasor multiplication would be incorrect. The correct DC value is given by: Re(½ J.B*)

This means that with a 15kHz applied field, the Lorentz force is a 30kHz sinusoid. Ščepanskis and our models use this average value. If we want to use the actual oscillating Lorentz Force, the simulations would be very expensive.

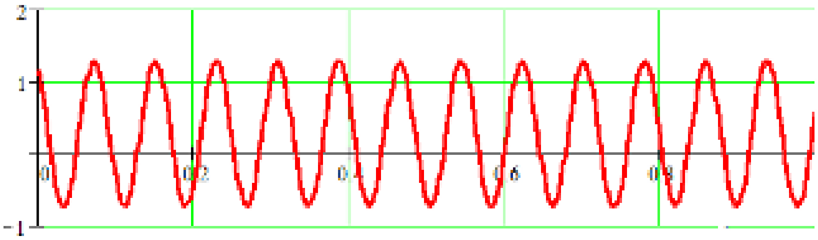

Figure 28. Lorentz force waveform (Note: the sinusoid is not centered on the y-axis).

Appendix D – Simulation Properties for the Two Cases

I. Case: ICF2 setup (Ščepanskis et al.[61])

Crucible Wall Height Inside	100	mm	
Crucible Wall Thickness	2	mm	
Crucible Base Thickness	2	mm	
Melt Diameter/CrucibleID	90	mm	
Melt Height	100	mm	
Coil Number of Turns	6		
Coil ID (melt plus 2x wall)	110	mm	
Coil Wire OD	4	mm	
Coil Wire ID (if Hollow)	0.1	mm	
Coil Fq	4000	Hz	
Coil Current	432	Amp	
Coil Height	96	mm	Coil height, center of bottom coil to center of top coil
Crucible Base to Coil Base	10	mm	Lower edge of coil is 10 mm above the base of crucible
Coil Conductivity	58E6	S/m	Copper
Melt conductivity	1E6	S/m	Wood's metal 50% Bi – 26.7% Pb – 13.3% Sn – 10% Cd (Melting Point 70C)
Melt permeability (relative)	1		
Melt density	9400	Kg/m^3	At 70C
Melt dynamic viscosity	4.2E-3	Kg/ms	At 70C
Surface tension	0.46	N/m	Woods metal to air
Particle density (Fe)	7874	Kg/m^3	Conductive Fe particles, lighter than melt
Particle size	250	microns	
Air density	1.2	Kg/m^3	20°C, 1 atm

Air density	~0.9	Kg/m³	70°C, 1 atm

II. Case Lab/Uranium setup

Crucible Wall Height Inside	91.4	mm	
Crucible Wall Thickness	13.49	mm	
Crucible Base Thickness	17.46	mm	
Melt Diameter/CrucibleID	41.3	mm	
Melt Height	76.2	mm	
Coil Number of Turns	10		
Coil ID (melt plus 2x wall)	68.25	mm	
Coil Wire OD	6	mm	
Coil Wire ID (if Hollow)	4	mm	
Coil Fq	15000	Hz	
Coil Current	450	Amp	
Coil Height	68.5	mm	Coil height, center of bottom coil to center of top coil
Crucible Base to Coil Base	9	mm	Lower edge of coil is 10 mm above the base of crucible
Coil Conductivity	58E6	S/m	Copper
Melt conductivity	1.67E6	S/m	Uranium (Melting Point 1400°C)
Melt relative permeability	1		Magnetic relative permeability is not very different from that of vacuum
Melt density	19000	Kg/m³	At 1400°C
Melt dynamic viscosity	4.35	mPas	At 1400°C
Surface tension	0.8	N/m	Molten Uranium to air
Particle density (UC)	13000	Kg/m³	Uranium Carbide, lighter than melt
Particle size	1	micron	
Gas density	1.2	Kg/m³	20C, 101 kPa
Gas density	1.15	Kg/m³	1400 °C

Pacific Northwest
National Laboratory

902 Battelle Boulevard
P.O. Box 999
Richland, WA 99354
1-888-375-PNNL (7665)

www.pnnl.gov